coatings

MDPI

Article

Single-Layer MoS_2: A Two-Dimensional Material with Negative Poisson's Ratio

Yucheng Zhu [1], Xiaofei Cao [1], Yuan Tan [1], Yao Wang [2], Jun Hu [1,*], Baotong Li [3] and Zhong Chen [4]

[1] School of Chemical Engineering, Northwest University, Xi'an 710069, China
[2] Engineering Research Center of Alternative Energy Materials and Devices, Ministry of Education, Sichuan University, Chengdu 610065, China
[3] Key Laboratory of Education Ministry for Modern Design and Rotor-Bearing System, Xi'an Jiaotong University, Xi'an 710049, China
[4] School of Materials Science and Engineering, Nanyang Technological University, Singapore 639798, Singapore
* Correspondence: hujun@nwu.edu.cn

Abstract: Negative Poisson's ratio (NPR) materials have broad applications such as heat dissipation, vibration damping, and energy absorption because of their designability, lightweight quality, and high strength ratio. Here, we use first-principles calculations to find a two-dimensional (2D) auxetic material (space group $R\bar{3}m$), which exhibits a maximum in-plane NPR of -0.0846 and a relatively low Young's modulus in the planar directions. Calculations show that the NPR is mainly related to its unique zigzag structure and the strong interaction between the 4d orbital of Mo and the 3p orbital of S. In addition, molecular dynamics (MD) simulations show that the structure of this material is thermodynamically stable. Our study reveals that this layered MoS_2 can be a promising 2D NPR material for nanodevice applications.

Keywords: two-dimensional materials; DFT; elastic constants; negative Poisson's ratio; first-principles calculations; strong p-d orbital interactions

Citation: Zhu, Y.; Cao, X.; Tan, Y.; Wang, Y.; Hu, J.; Li, B.; Chen, Z. Single-Layer MoS_2: A Two-Dimensional Material with Negative Poisson's Ratio. *Coatings* **2023**, *13*, 283. https://doi.org/10.3390/coatings13020283

Academic Editors: Emerson Coy and Andrey V. Osipov

Received: 25 November 2022
Revised: 17 January 2023
Accepted: 20 January 2023
Published: 26 January 2023

1. Introduction

Young's modulus is a physical quantity that characterizes the resistance of a material to tensile or compressive forces within the limits of elasticity [1,2]. Poisson's ratio (PR) is defined as the ratio of the transversal strain to the strain along the applied stress direction when the material is deformed elastically [3]. Generally, PR, by definition, is positive for most commonly available engineering materials when the applied strain and the resultant transverse strain have opposite signs [4]. NPR materials refer to the phenomenon of lateral expansion when subjected to uniaxial tensile stress [5]. NPR materials possess certain advantageous properties including strong designability [6], light weight [7], high strength ratio [8], and high damping [9], and moreover have good performance in heat dissipation [10], vibration reduction [11], and energy absorption [12]. These excellent mechanical properties greatly expand the scope of the application of NPR materials. At present, there are broad application prospects in the fields of aerospace, equipment armor, intelligent manufacturing, coating materials, and so on.

Quantum confinement caused by the low-dimensional effect of two-dimensional (2D) materials makes them more prone to NPR [13–16]. Therefore, it is possible to find new 2D NPR materials for novel nanomaterial applications. Until now, some NPR materials have been identified, such as black phosphorus (BP) [17], Be_5C_2 [18], SnSe [19], TiN [20], α-phosphorene [21], δ-phosphorene [22], Cd_2C [23], Zn_2C [24], and Ag_2S [25]. However, the number is still small considering the numerous materials [26,27] that have been discovered and investigated [28]. MoS_2 is one of the well-known materials possessing several different configurations, which have different structures. MoS_2 [29] is a material composed of two chemical elements, molybdenum and sulfur, with excellent optical, electrical,

magnetic, force, and thermal properties, and is widely used in energy storage, catalysis, semiconductors, lubrication, and other fields. It is notable that in the mechanical properties, both positive and negative PR are present in the MoS_2 configuration, which is rare for the same material of other compounds. It has been reported that MoS_2 has both positive and negative PR, and small changes in the structure will greatly affect the PR. Yu et al. [30], in 2017, reported 42 1T-type crystals in which the presence of NPR for MoS_2 was suggested, while Hung et al. [31], in 2018, reported three different structures of MoS_2 with positive and negative PR. These results coincide with our calculations. However, for the same material (MoS_2), there is no exact explanation of what causes its many configurations to have both positive and negative PR. The main reason is that there is a general lack of understanding of the mechanism of NPR materials. Therefore, in-depth analysis from the perspective of electron interaction is needed to understand the mechanisms behind the formation of NPR materials. Such understanding is important for the search and design of new materials with widened application prospects.

There are three different phases of monolayer MoS_2: 1T-phase, 1H-phase, and 1T'-phase MoS_2, respectively [32]. To investigate in-depth the formation mechanism behind NPR, 1T-phase MoS_2 with NPR and three other materials were selected for comparison, and their respective Young's modulus, PR, and projected density of states (PDOS) were calculated. Their geometries and electronic structures were compared to analyze their effects on the NPR generation of the materials, and the mechanism of NPR formation was demonstrated in terms of both geometric deformation and electronic structure. Finally, the formation mechanism of NPR materials was further investigated from the perspective of layer spacing and intralayer forces.

2. Computational Methods

All calculations were performed using the CASTEP (version 8.0.) [33,34] module of the Materials Studio package. During the computational process, self-consistent periodic density functional theory (DFT) [35,36] was adopted by the Generalized Gradient Approximation (GGA) method using the Perdew–Burke–Ernzerhof (PBE) exchange–correlation functional [37]. The energy cutoff was 340 eV and the Self-Consistent Field (SCF) tolerance was 5.0×10^{-7} eV atom^{-1}. The convergence criteria for max force, max displacement, max stress, and energy were set to lower than 0.01 eV Å^{-1}, 5.0×10^{-4} Å, 0.02 GPa, and 5.0×10^{-6} eV atom^{-1}, separately [38]. The k-point meshes were set as $5 \times 5 \times 5$ for the bulk. The Young's modulus $Y(\theta)$ and PR $\upsilon(\theta)$ could be indicated as follows [39]:

$$Y(\theta) = \frac{C_{11}C_{22} - C_{12}^2}{C_{11}sin^4\theta + Asin^2\theta cos^2\theta + C_{22}cos^4\theta}$$
$$\upsilon(\theta) = \frac{C_{12}sin^4\theta - Bsin^2\theta cos^2\theta + C_{12}cos^4\theta}{C_{11}sin^4\theta + Asin^2\theta cos^2\theta + C_{22}cos^4\theta}$$

where C_{ij} are the elastic constants, $A = \left(C_{11}C_{22} - C_{12}^2\right)/C_{66} - 2C_{12}$ and $B = C_{11} + C_{22} - \left(C_{11}C_{22} - C_{12}^2\right)/C_{66}$. In order to verify the calculation, we calculated the elastic constant of $MoTe_2$, which was in agreement with the available theoretical values [40]. The calculated elastic constants of MoS_2 and $MoTe_2$ are included in Table S1. The molecular dynamics (MD) simulation in the NVT (Number of particles, Volume, and Temperature) ensemble was performed at 300 K with a $3 \times 3 \times 1$ supercell for 6ps with a time step of 1fs. MD was performed with periodic boundary conditions. In order to ensure the accuracy of the simulation, a vacuum layer of 15 Å was added to the four models to eliminate a certain degree periodic interaction and the bottom layer of MoS_2 was fixed in the calculation process. The force field used in the MD simulation was a universal force field (UFF). UFF was applied to optimize the model and assign charges to ensure the accuracy of the calculation results. The designation of the algorithm used in the geometry optimization calculations was a quasi-Newton method. The initial model was minimized by the quasi-Newton method until the gradient was less than 0.1 kcal/mol. All materials involved were from the crystallographic database: materials project.

3. Results and Discussion

1T-phase MoS_2 is a member of transition metal dichalcogenides (TMD) [41]. The unique zigzag structure of MoS_2 brings many unique mechanical properties. In the current work, we explore the mechanical properties by computing the planar Young's modulus $Y(\theta)$ and PR $\upsilon(\theta)$. Results are drawn in Figure 1a. Young's modulus $Y(\theta)$ is a physical quantity that describes a material's ability to resist elastic deformation. More rigid materials have a higher Young's modulus. As Figure 1a shows, Young's modulus of MoS_2 does not show anisotropy, which means that the mechanical response to the same strain varies little along different in-plane directions. Young's modulus attains a maximum value of 183.1 GPa at $\theta = 62°$, 118°, 224°, and 298° , and a minimum value of 178.9 GPa at $\theta = 0°$ and 180°. This indicates that MoS_2 exhibits moderate deformation-resistant stiffness in all directions. For comparison, Young's modulus of graphene [42] and TiS_2 [43] is added in the bar chart of Figure 1a. Compared to these two well-known materials, Young's modulus of MoS_2 is comparatively low. This means that MoS_2 exhibits considerable elastic compliance, which can be traced to its special atomic structure (to be discussed later). The PR $\upsilon(\theta)$ of MoS_2 is shown in Figure 1b. It exhibits an NPR in the whole region and reaches the highest value of -0.0846 at 46°, 134°, 226°, and 314°, indicating that MoS_2 is an auxetic material. The planar NPR value is bigger than that of penta-graphene ($\upsilon = -0.068$) [44], PN ($\upsilon = -0.078$) [45], and borophene ($\upsilon = -0.053$) [46].

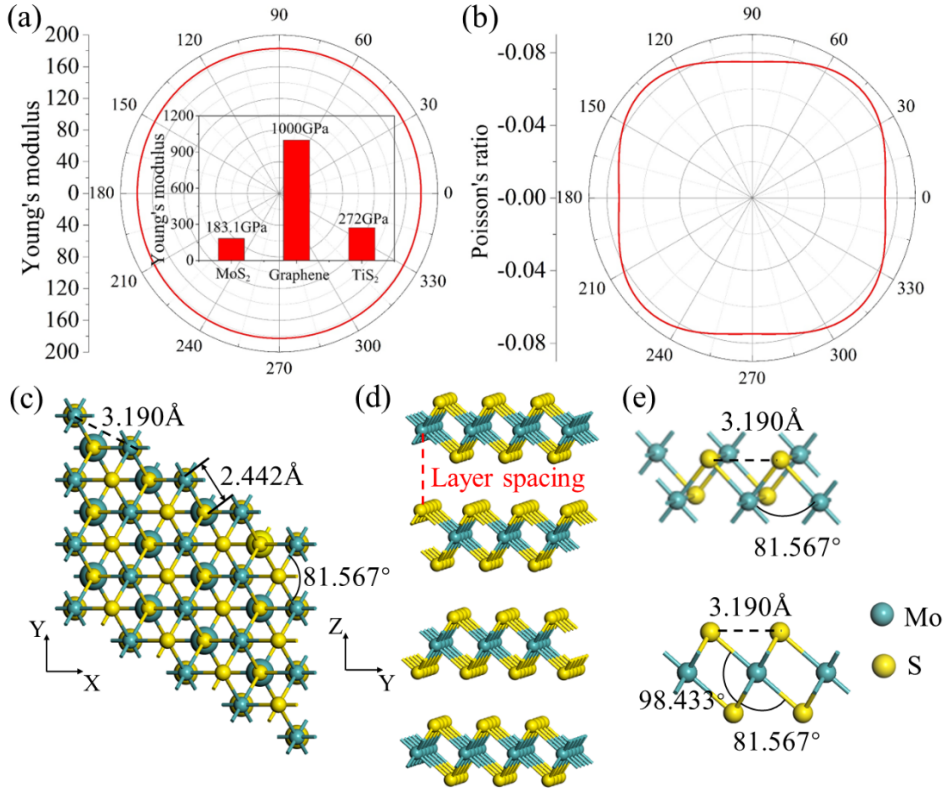

Figure 1. (**a**) Young's modulus and (**b**) PR of MoS_2 as a function of the angle θ. θ = 0° corresponds to the *X*-axis. The comparative Young's modulus of the three materials is plotted in the Young's modulus diagram of MoS_2. (**c**) Top view of bulk MoS_2 (space group $R\bar{3}m$). The partially enlarged atoms in the figure are the obscured parts of the layered MoS_2, and the red dashed lines indicate the spacing between the layers. (**d**) Side view of MoS_2. (**e**) Local enlargement of the side view of the monolayer MoS_2.

The crystal structure of bulk MoS_2 is displayed in Figure 1c. The band structure as well as the density of states (DOS) of MoS_2 is plotted in Figure S1. It could be regarded as a laminar structure in which the zigzag layers are linked by the Mo-S bonds. Its primitive

cell consists of six sulfur atoms and three molybdenum atoms in a trigonal crystal system. The lattice constants are a = b = 3.190 Å, and the space group is R$\bar{3}$m [47]. From the crystal structure diagram, the structure of this material can be considered as a network of herringbone Mo-S atomic chains in two directions, one along the monoclinic lattice and the other perpendicular to the lattice direction. The angles of S-Mo-S along these two directions are 81.567° and 98.433°, respectively (See Figure 1e).

To investigate how the atomic geometry affects PR, three additional materials were selected for comparison: the MoS_2 with zigzag structure (space group $P6_3/mmc$), the MoS_2 without the special undulations (space group F$\bar{4}$3m), and the WS_2 with the same R$\bar{3}$m space group but different elements. The calculated results are plotted in Figures 2 and S2. The lattice constants and the atomic coordinates in every cell after optimization are included in Table S2. Clearly, among the three compared materials, MoS_2 with space group F$\bar{4}$3m has no obvious zigzag geometry, and it shows a positive Poisson's ratio (PPR). This is in agreement with the previous conclusion that the unique sawtooth-like geometry is necessary for an NPR to occur [48]. However, the PR of the other two materials with similar sawtooth geometries (MoS_2, space group $P6_3/mmc$; WS_2, space group R$\bar{3}$m) is also positive. This suggests the NPR is not only related to the material geometry. Other factors may play a role too.

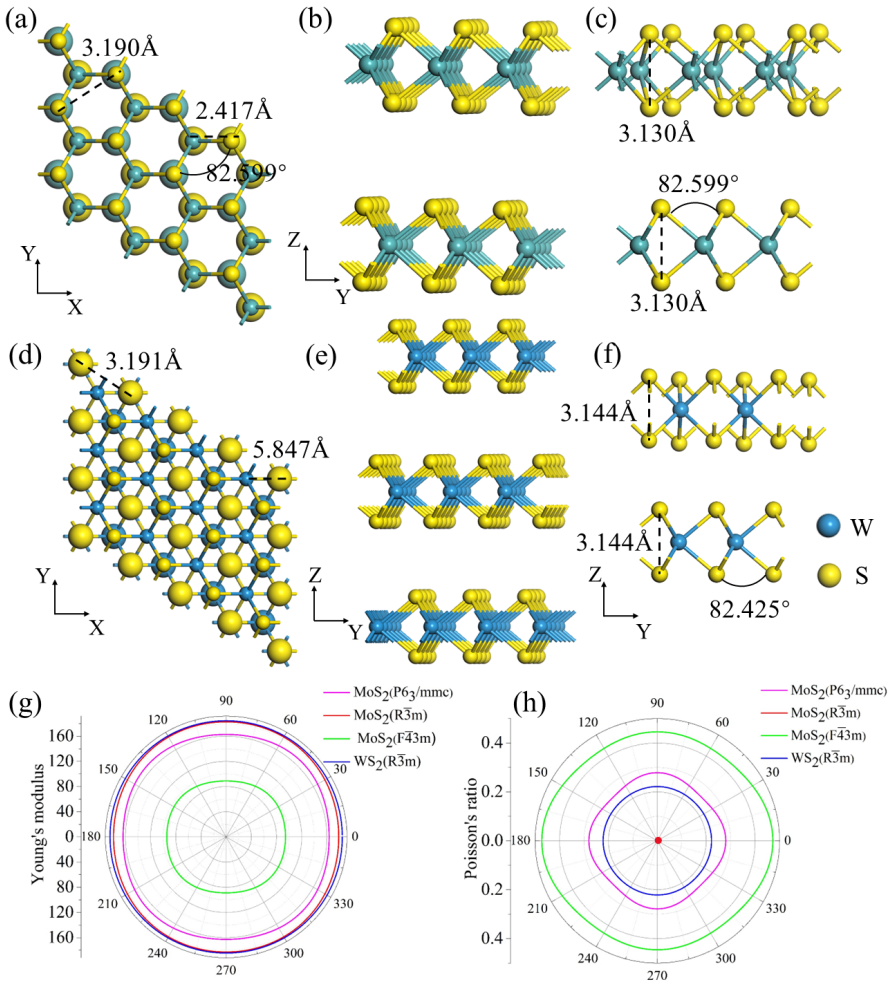

Figure 2. (**a**) Structural snapshots (top view) of MoS_2 (space group $P6_3/mmc$). (**b**) Side view of MoS_2 (space group $P6_3/mmc$). (**c**) Local enlargement of a side view of the monolayer MoS_2 (space group $P6_3/mmc$). (**d**) Structural snapshots (top view) of WS_2 (space group R$\bar{3}$m). (**e**) Side view of WS_2 (space group R$\bar{3}$m). (**f**) Local enlargement of the side view of the monolayer WS_2 (space group R$\bar{3}$m). (**g**) Summary graph of Young's modulus and (**h**) PR of four materials. To show their structure more clearly, the above materials are enlarged for the part of the atoms that are obscured between the layers; this does not mean that they are different in size.

To gain a more in-depth insight into the deformation mechanism behind the NPR, we further analyzed the electronic interactions. We calculated the PDOS of the four materials to observe their electronic structures, as shown in Figure 3. The PDOS peak shape and position of the 4d orbital of the Mo atom and the 3p orbit of the S atom are similar in energy, indicating the strong orbital interaction of the Mo atom and S atom (the yellow highlighted portion of Figure 3a). It can be seen that both sets of orbitals overlap above the Fermi energy level, indicating that the atoms are antibonding. It is well-known that the bonding state leads to attractive interactions, while the possession of the antibonding state causes repulsive interactions. This is most likely a key factor in the generation of NPR for MoS_2. Moreover, the MoS_2 that shows an NPR has an overlap area of 5.854 above the Fermi level, while the other three materials showing PPR have overlaps of 1.807, 0, and 2.508 above the Fermi level, respectively, which all indicate that their coupling is not as strong as that of the NPR materials at the p-d orbitals.

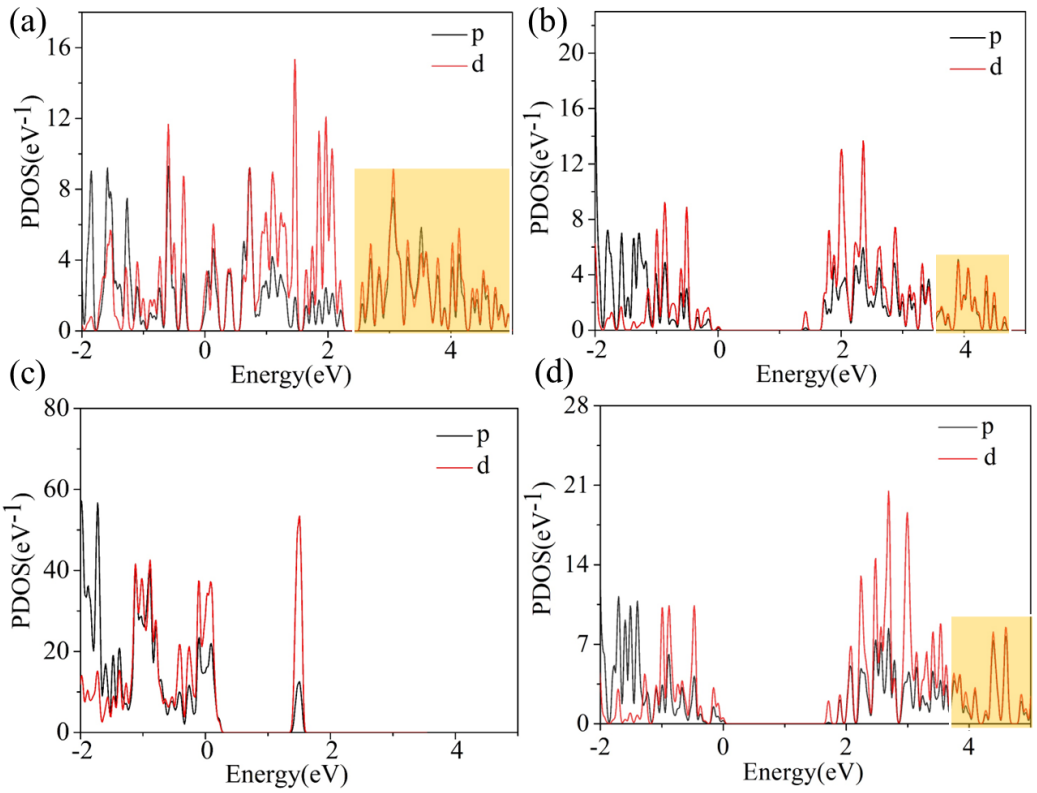

Figure 3. (**a**) PDOS of MoS_2(space group $R\bar{3}m$). The p-d orbital coupling is reflected in the overlap of its PDOS. The area of overlap above the Fermi level is 5.854. (**b**) PDOS of MoS_2 (space group $P6_3/mmc$). The area of overlap above the Fermi level is 1.807. (**c**) PDOS of MoS_2(space group $F\bar{4}3m$). The area of overlap above the Fermi level is 0. (**d**) PDOS of WS_2(space group $R\bar{3}m$). The area of overlap above the Fermi level is 2.508. The Fermi level is set to 0. The yellow highlighted part indicates the overlapping part of the PDOS of the materials.

Figure 3d indicates that the interaction of the p orbital and d orbital of WS_2 is significantly weaker than MoS_2 in the energy range of 0 to 6 eV. Although both MoS_2 (space group $R\bar{3}m$) and WS_2 (space group $R\bar{3}m$, and the value of PR is 0.25 in Figure 2h) share the same space group, there are differences in their electronic structures that lead to very different results. Therefore, the electronic structure is one of the characteristics of the NPR of MoS_2. In summary, an NPR material should have a special geometry in terms of structure (i.e., undulating structure), while in microscopic terms, it should have a strong enough coupling between different orbitals (i.e., electron interaction), and the atoms are anti-bonding (the atoms will tend to interact with each other in a repulsive manner). Materials that have all these characteristics will have a much higher probability of NPR.

Electronic interactions can be divided into interlayer and intralayer based on the geometric configuration of MoS_2. Furthermore, we investigated how the electronic structure affects the interatomic forces that lead to the NPR in the material. Figure 4a displays the structure of the initial MoS_2, and Figure 4b displays the structure with the new alignment rebuilt by cleaving the (0 0 1) surface of MoS_2. The difference between them is that the initial structure is staggered and aligned, while the modeled structure is overlapping and aligned. By varying their layer spacing, it is possible to investigate how much the interlayer forces of these two very different alignments contribute to the generation of NPR. As illustrated in Figure 4c, the PR of the material varies in value but remains negative overall. The PR varies from −0.67 to −0.82 and from −0.10 to −0.13, with a moderate variation. It indicates that the value of the PR does not change greatly with an increase in the layer spacing, indicating that the layer spacing has almost no impact on the NPR of the material. Therefore, the interatomic forces caused by the intralayer electronic structure of monolayer MoS_2 may be the dominant factor.

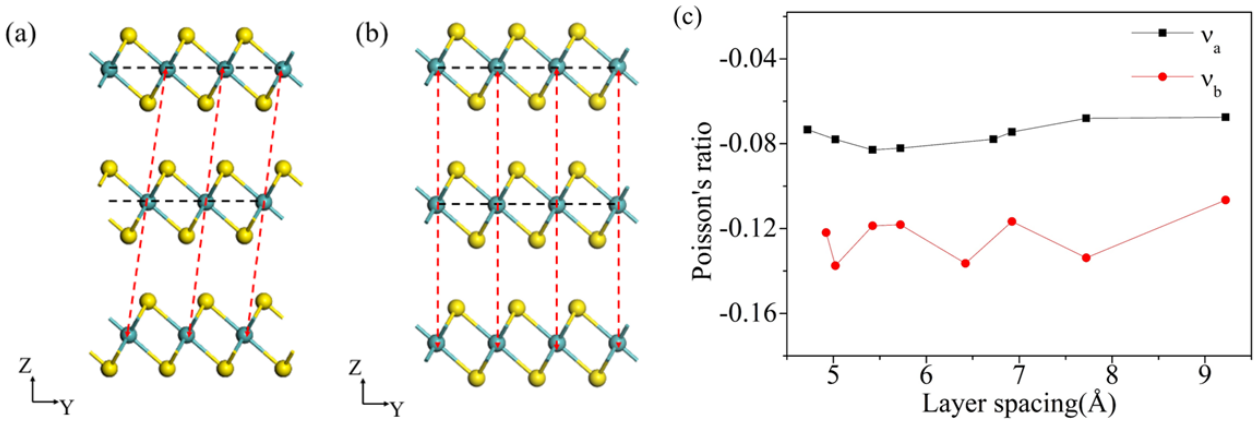

Figure 4. (**a**) The original structure of MoS_2. (**b**) The structure with overlapping alignment between layers of MoS_2. (**c**) The relationship between PR and layer spacing for two different arrangements of structures.

Based on the above analyses, the force generated by the electronic structure between the layers has little effect on the deformation of the whole structure. In the next step, we applied a strain to the single-layer MoS_2 (space group $R\bar{3}m$) and observed how the interaction between the electrons in the structure within the layer affected the material's PR. Figure 5a shows a sketch of the original structure with a monolayer of MoS_2. This is a material with a folded structure with upper and lower pyramidal shapes. Figure 5b shows a schematic of the structure after it has been stretched. When two Mo atoms, Mo_A and Mo_B, are pulled in the *Y*-axis, the structure produces a force of compression in the *Z*-axis because of the intense interaction of the p-d orbitals, resulting in the structure being compressed in that direction and pulled in the *X*-axis. The bond angles of ∠CAB and ∠CBA are reduced behind the deformation. In principle, the change of ∠CAB is not impacted by the stretching of the Mo_A and Mo_B atoms, which is only related to the reciprocal action of the p-d orbitals. That is, the displacements occurring in the Mo_A and Mo_B during the deformation are only relevant to the strength inside the cell. Therefore, the angular variation of ∠CAB could be used to describe the mechanical behavior generated within the cell. When a 5% stretch strain is applied in the *Y*-axis, the bond angle of ∠CAB decreases from 49.216° to 45.376° (a decrease of 3.84°), and the interplanar spacings d_{AC} and d_{CE} decrease by 0.052 Å and 0.039 Å, respectively. The strong coupling of the p-d orbitals causes a large amount of strain energy generated during deformation to be stored in the reduced ∠CAB and ∠CBA, and this strain energy is released by increasing the distance between Mo atoms D and Mo atoms A, leading to an NPR. This confirms the above inference that the p-d orbital interactions lead to a planar NPR in monolayered MoS_2. Further observing the PDOS of MoS_2 in Figure 3a, the p-orbital overlaps with the d-orbital at positions above the Fermi

level, which indicates that the metal atoms exhibit a strong antibonding property, which leads to mutual repulsion between the atoms. As a result, the NPR phenomenon appears.

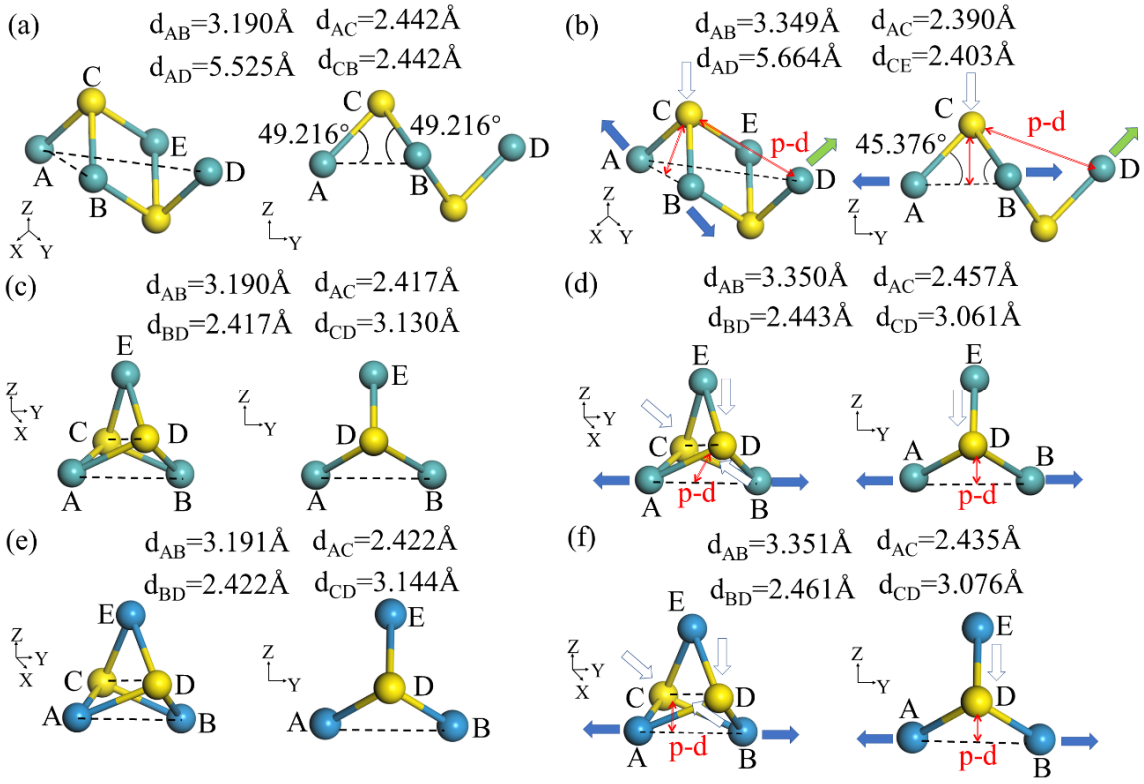

Figure 5. (**a**) Structure of single-layer MoS_2 (space group $R\bar{3}m$) without strain. (**b**) Structure of single-layer MoS_2 (space group $R\bar{3}m$) after strain is applied. The force is applied along the *Y*-axis. The red arrow indicates p-d orbital interaction and the green arrow shows the result of the final movement of MoS_2. (**c**) Structure of single-layer MoS_2 (space group $P6_3/mmc$) without strain. (**d**) Structure of single-layer MoS_2 (space group $P6_3/mmc$) after strain is applied. (**e**) Structure of single-layer WS_2 (space group $R\bar{3}m$) without strain. (**f**) Structure of single-layer WS_2 (space group $R\bar{3}m$) after strain is applied.

For comparison, we applied tensile strain on both WS_2 (space group $R\bar{3}m$) and MoS_2 (space group $P6_3/mmc$), which exhibited PPR. Figure 5 shows that after applying a tensile strain, the whole structure shrunk to a certain extent. Combined with the previous analysis, these two materials used as comparisons have a weaker coupling in their p-d orbitals, resulting in a reduction in the strain energy that can be stored in the bond angles during tensile strain. As a result, the changing bond angles release less energy and have a reduced effect on the surrounding atoms when the structure shrinks. The PDOS of the two compared materials did not exhibit strong antibonding properties and the atoms did not tend to repel each other, meaning they ended up exhibiting PPR. To better verify our speculation, we also calculated PDOS for four other NPR materials, and the outcomes are listed in Figure S4. It is clear from the figure that the four NPR materials have similar degrees of overlap in the positions of the peaks and energies of the PDOS, indicating that they all have strong interactions in their p-d orbitals. Such a comparison shows that the change in interatomic forces due to the interaction between p-d orbitals is a major factor in the NPR behavior of the 2D materials, which can be used as a feature for screening NPR materials. More specifically, the NPR of single-layer MoS_2 is related to the strong coupling between the 4d orbital of the Mo atom and the 3p orbital of the S atom, and the antibonding orbits of the atoms present. This eventually causes the interaction forces between the Mo and S atoms to tend to repel each other, leading to their extension and triggering NPR.

Finally, we performed molecular dynamics (MD) simulations at 500 K for 6 ps with NVT (Number of particles, Volume, and Temperature) ensemble to evaluate the structural stability of MoS_2 [49]. In the process of structural evolution, temperature fluctuations and the mean potential energy of atoms are displayed in Figure 6. Throughout the simulation process, the changes in potential energy remained near the average. Figure 6 and Figure S5 give three different configurations of MoS_2 and WS_2 structural snapshots at the end of 6 ps. The diagram shows that the geometry is well-saved and no significant structured fractures are observed, which indicates that the structure of MoS_2 is stable. The calculated elastic constants of the 2D molybdenum disulfide meet the Born−Huang criteria [50], in which C_{11}, C_{22}, $C_{66} > 0$ and $C_{11} + C_{22} - 2C_{12} > 0$. Judging from the data in Table S1, it is confirmed that the MoS_2 structure is stable.

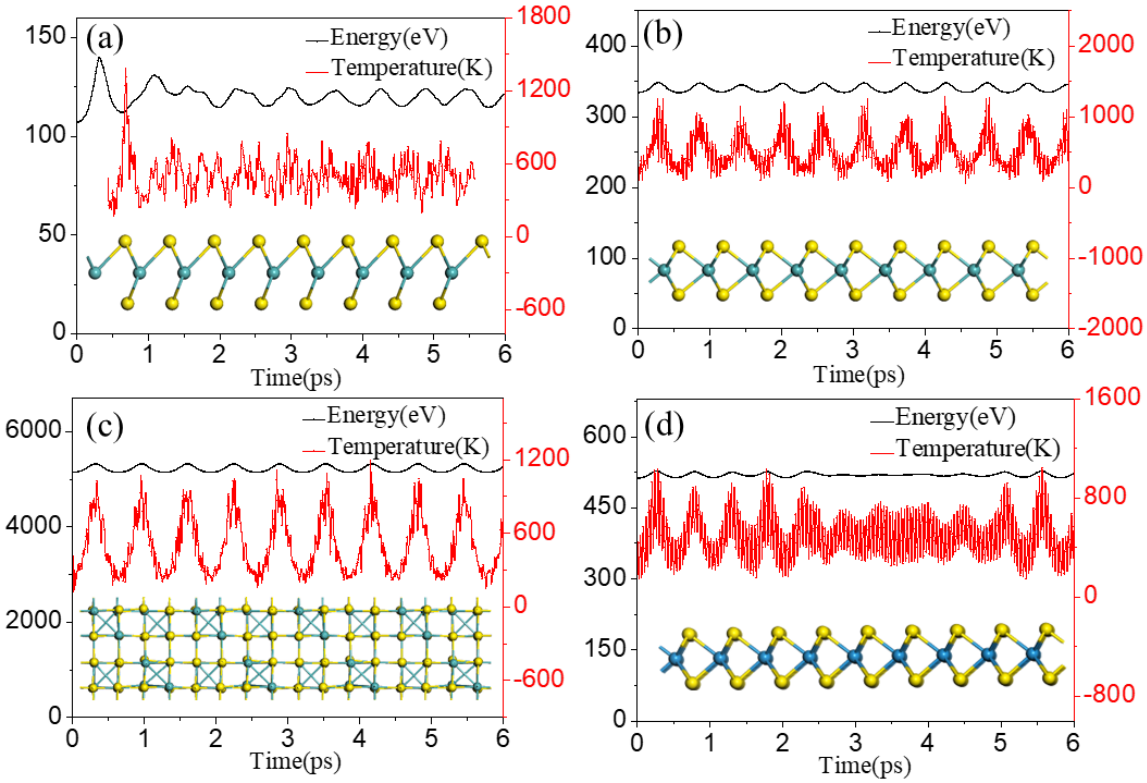

Figure 6. Structural snapshots (side view) of the (**a**) MoS_2 (space group $R\bar{3}m$) (**b**) MoS_2 (space group $P6_3/mmc$) (**c**) MoS_2 (space group $F\bar{4}3m$) and (**d**) WS_2 (space group $R\bar{3}m$), with the evolution of the mean potential energy and temperature per atom in MD (molecular dynamics) simulations at 500 K and 6 ps.

4. Conclusions

To sum up, we used first-principles calculations for the elastic constants of 2D molybdenum disulfides and have succeeded in finding a molybdenum disulfide with NPR (space group $R\bar{3}m$). This serrated structure with unique layer overlap exhibits a separate NPR of $\upsilon_x = -0.0736$ and $\upsilon_y = -0.0750$ in the *X*- and *Y*-axis. In addition, we explored the effect of layer spacing on its NPR behavior. Finally, we found that the unusual NPR behavior of single-layer MoS_2 is linked to its unique geometry and the strong interaction between the 4d orbitals of Mo and the 3p orbitals of S. Moreover, we also found that the strong coupling of p-d orbitals and the zigzag structure of the antibonding state are notable features for screening 2D NPR materials. These discoveries provide insight into the influence of the geometry and electronic structure of 2D molybdenum disulfide on the mechanical performance of the material. These results could propel progress in the screening and design of other 2D materials in the future.

Supplementary Materials: The following supporting information can be downloaded at https://www.mdpi.com/article/10.3390/coatings13020283/s1. Figure S1: The band structure and the DOS of MoS_2. The energy band structure describes the energy that electrons are forbidden or allowed to carry, which is caused by the diffraction of quantum dynamics electron waves in a periodic lattice. The energy band structure of a material determines various properties, especially its electronic and optical properties; Figure S2: MoS_2 (space group $F\bar{4}3m$); Figure S3: Comparison graphs of Young's modulus and Poisson's ratio for the four materials; Figure S4: Four negative Poisson's ratio materials and their PDOS plots. (a) MoS_2 (space group $P\bar{3}m1$). (b) MoS_2 (space group $I\bar{4}2d$). (c) MoSe (space group $P\bar{6}m2$). (d) WS_2 (space group $I\bar{4}2d$); Figure S5: Structural snapshots (side view) of the (a) MoS_2 (space group $R\bar{3}m$) (b) MoS_2 (space group $P6_3/mmc$) (c) MoS_2 (space group $F\bar{4}3m$) and (d) WS2 (space group $R\bar{3}m$) with the evolution of the average potential energy and temperature per atom in AIMD simulations at 500 K and 6 ps; Table S1: The calculated elastic constants (units of GPa) of 2D MoS_2 and $MoTe_2$; and Table S2: Structural information of three configurations of MoS_2.

Author Contributions: Conceptualization, J.H.; methodology, Y.Z.; software, Y.Z.; validation, Y.Z., Y.T. and X.C.; formal analysis, Y.Z.; investigation, J.H.; resources, J.H.; data curation, Y.Z.; writing—original draft preparation, Y.Z.; writing—review and editing, Z.C.; visualization, J.H. and Y.W.; supervision, B.L. and Y.W.; project administration, B.L.; funding acquisition, B.L. All authors have read and agreed to the published version of the manuscript.

Funding: Financial support was received from the National Natural Science Foundation of China (Grant Number 21676216); the Preferential Funding Project for Scientific and Technological Activities of Overseas Chinese in Shaanxi Province (Grant Number 2021008); and the Center for High-Performance Computing of Northwestern Polytechnical University, China.

Institutional Review Board Statement: Not applicable.

Informed Consent Statement: Not applicable.

Data Availability Statement: Not applicable.

Conflicts of Interest: The authors declare that they have no known competing financial interests or personal relationships that could have appeared to influence the work reported in this paper.

References

1. Huang, C.; Zhou, J.; Wu, H.; Deng, K.; Jena, P.; Kan, E. Quantum anomalous Hall effect in ferromagnetic transition metal halides. *Phys. Rev. B* **2017**, *95*, 45113. [CrossRef]
2. Zhang, G.; Qin, G.; Zhang, F. Effects of Internal Relaxation of Biaxial Strain on Structural and Electronic Properties of $In_{0.5}Al_{0.5}N$ Thin Film. *Coatings* **2022**, *12*, 598. [CrossRef]
3. Evans, K.E.; Nkansah, M.A.; Hutchinson, I.J.; Rogers, S.C. Molecular network design. *Nature* **1991**, *353*, 124. [CrossRef]
4. Yuan, R.; Zhou, Y.; Fan, X.; Lu, Q. Negative-Poisson-Ratio polyimide aerogel fabricated by tridirectional freezing for High- and Low-Temperature and Impact-Resistant applications. *Chem. Eng. J.* **2022**, *433*, 134404. [CrossRef]
5. Yang, W.; Li, Z.; Shi, W.; Xie, B.; Yang, M. Review on auxetic materials. *J. Mater. Sci.* **2004**, *39*, 3269–3279. [CrossRef]
6. Ting, T.C.T.; Chen, T. Poisson's ratio for anisotropic elastic materials can have no bounds. *Q. J. Mech. Appl.* **2005**, *58*, 73–82. [CrossRef]
7. Hu, H.; Silberschmidt, V. A composite material with Poisson's ratio tunable from positive to negative values: An experimental and numerical study. *J. Mater. Sci.* **2013**, *48*, 8493–8500. [CrossRef]
8. Gao, Z.; Dong, X.; Li, N.; Ren, J. Novel Two-Dimensional Silicon Dioxide with in-Plane Negative Poisson's Ratio. *Nano Lett.* **2017**, *17*, 772–777. [CrossRef] [PubMed]
9. Kaminakis, N.T.; Stavroulakis, G.E. Topology optimization for compliant mechanisms, using evolutionary-hybrid algorithms and application to the design of auxetic materials. *Compos. Part B* **2012**, *43*, 2655–2668. [CrossRef]
10. Blackburn, S.; Wilson, D.L. Shaping ceramics by plastic processing. *J. Eur. Ceram. Soc.* **2008**, *7*, 1341–1351. [CrossRef]
11. Lipsett, A.W.; Beltzer, A.I. Reexamination of dynamic problems of elasticity for negative Poisson's ratio. *J. Acoust. Soc. Am.* **1988**, *84*, 2179. [CrossRef]
12. Lakes, R.; Elms, K. Indentability of Conventional and Negative Poisson's Ratio Foams. *J. Compos. Mater.* **1993**, *27*, 1193. [CrossRef]
13. Li, X.; Gao, L.; Zhou, W.; Wang, Y.; Lu, Y. Novel 2D metamaterials with negative Poisson's ratio and negative thermal expansion. *Extrem. Mech. Lett.* **2019**, *30*, 100498. [CrossRef]
14. Demir, H.; Cosgun, A.E. The Effect on Energy Efficiency of Yttria-Stabilized Zirconia on Brass, Copper and Hardened Steel Nozzle in Additive Manufacturing. *Coatings* **2022**, *12*, 690. [CrossRef]
15. Khomenko, V.; Butenko, O.; Chernysh, O.; Barsukov, V.; Suchea, M.P.; Koudoumas, E. Electromagnetic Shielding of Composite Films Based on Graphite, Graphitized Carbon Black and Iron-Oxide. *Coatings* **2022**, *12*, 665. [CrossRef]

16. Buet, E.; Braun, J.; Sauder, C. Influence of Texture and Thickness of Pyrocarbon Coatings as Interphase on the Mechanical Behavior of Specific 2.5D SiC/SiC Composites Reinforced with Hi-Nicalon S Fibers. *Coatings* **2022**, *12*, 573. [CrossRef]
17. Jiang, J.; Park, H.S. Negative Poisson's ratio in single-layer black phosphorus. *Nat. Commun.* **2014**, *5*, 4727. [CrossRef]
18. Wang, Y.; Li, F.; Li, Y.; Chen, Z. Semi-metallic Be_5C_2 monolayer global minimum with quasi-planar pentacoordinate carbons and negative Poisson's ratio. *Nat. Commun.* **2016**, *7*, 11488. [CrossRef] [PubMed]
19. Zhang, L.C.; Qin, G.; Fang, W.Z.; Cui, H.J.; Zheng, Q.R.; Yan, Q.B.; Su, G. Tinselenidene: A Two-dimensional Auxetic Material with Ultralow Lattice Thermal Conductivity and Ultrahigh Hole Mobility. *Sci. Rep.* **2016**, *6*, 19830. [CrossRef]
20. Zhou, L.; Zhuo, Z.; Kou, L.; Du, A.; Tretiak, S. Computational Dissection of Two-Dimensional Rectangular Titanium Mononitride TiN: Auxetics and Promises for Photocatalysis. *Nano Lett.* **2017**, *17*, 4466–4472. [CrossRef]
21. Qin, G.; Yan, Q.B.; Qin, Z.; Yue, S.Y.; Cui, H.J.; Zheng, Q.R.; Su, G. Hinge-like Structure Induced Unusual Properties of Black Phosphorus and New Strategies to Improve the Thermoelectric Performance. *Sci. Rep.* **2015**, *4*, 6946. [CrossRef]
22. Wang, H.; Li, X.; Li, P.; Yang, J. δ-Phosphorene: A Two-Dimensional Material with a Highly Negative Poisson's Ratio. *Nanoscale* **2017**, *9*, 850–855. [CrossRef]
23. Meng, L.B.; Ni, S.; Zhang, Y.J.; Li, B.; Zhou, X.W.; Wu, W.D. Two-Dimensional Zigzag-Shaped Cd_2C Monolayer with a Desirable Bandgap and High Carrier Mobility. *J. Mater. Chem. C* **2018**, *6*, 9175–9180. [CrossRef]
24. Meng, L.; Zhang, Y.; Zhou, M.; Zhang, J.; Zhou, X.; Ni, S.; Wu, W. Unique Zigzag-Shaped Buckling Zn_2C Monolayer with Strain-Tunable Band Gap and Negative Poisson Ratio. *Inorg. Chem.* **2018**, *57*, 1958–1963. [CrossRef]
25. Peng, R.; Ma, Y.; He, Z.; Huang, B.; Kou, L.; Dai, Y. Single-Layer Ag_2S: A Two-Dimensional Bidirectional Auxetic Semiconductor. *Nano Lett.* **2019**, *19*, 1227–1233. [CrossRef]
26. Miró, P.; Audiffred, M.; Heine, T. An atlas of two-dimensional materials. *Chem. Soc. Rev.* **2014**, *43*, 6537–6554. [CrossRef] [PubMed]
27. Jiang, L.; Marconcini, P.; Hossian, M.S.; Qiu, W.; Evans, R.; Macucci, M.; Skafidas, E. A tight binding and k.p study of monolayer stanene. *Sci. Rep.* **2017**, *7*, 12069. [CrossRef] [PubMed]
28. Yan, Y.; Yan, J.; Gong, X.; Tang, X.; Xu, X.; Meng, T.; Bu, F.; Cai, D.; Zhang, Z.; Nie, G.; et al. All-in-one asymmetric micro-supercapacitor with Negative Poisson's ratio structure based on versatile electrospun nanofibers. *Chem. Eng. J.* **2022**, *433*, 133580. [CrossRef]
29. Mak, K.F.; Lee, C.; Hone, J.; Shan, J.; Heinz, T.F. Atomically Thin MoS_2: A New Direct-Gap Semiconductor. *Phys. Rev. Lett.* **2010**, *105*, 136805. [CrossRef]
30. Yu, L.; Yan, Q.; Ruzsinszky, A. Negative Poisson's ratio in 1T-type crystalline two-dimensional transition metal dichalcogenides. *Nat. Commun.* **2017**, *8*, 15224. [CrossRef]
31. Hung, N.T.; Nugraha, A.; Saito, R. Two-dimensional MoS_2 electromechanical actuators. *J. Phys. D Appl. Phys.* **2018**, *51*, 75306. [CrossRef]
32. Esteban-Puyuelo, R.; Sarma, D.D.; Sanyal, B. Complexity of mixed allotropes of MoS_2 unraveled by first-principles theory. *Phys. Rev. B* **2020**, *102*, 165412. [CrossRef]
33. Clark, S.J.; Segall, M.D.; Pickard, C.J.; Hasnip, P.J.; Probert, M.I.J.; Refson, K.; Payne, M.C. First principles methods using CASTEP. *Z. Kristallogr.* **2005**, *220*, 567–570. [CrossRef]
34. Segall, M.D.; Lindan, P.J.D.; Probert, M.I.J.; Pickard, C.J.; Hasnip, P.J.; Clark, S.J.; Payne, M.C. First-principles simulation: Ideas, illustrations and the CASTEP code. *J. Phys. Condens. Matter* **2002**, *14*, 27117. [CrossRef]
35. Fan, Y.; Xie, D.; Ma, D.; Jing, F.; Matthews, D.T.A.; Ganesan, R.; Leng, Y. Evaluation of the Crystal Structure and Mechanical Properties of Cu Doped TiN Films. *Coatings* **2022**, *12*, 652. [CrossRef]
36. Jacobsen, E.; Lyons, R. The sliding DFT. *IEEE Signal Process. Mag.* **2003**, *20*, 74–80.
37. Perdew, J.P.; Burke, K.; Ernzerhof, M. Generalized Gradient Approximation Made Simple. *Phys. Rev. Lett.* **1996**, *77*, 3865. [CrossRef]
38. Hu, J.; Chen, W.; Zhao, X.; Su, H.; Chen, Z. Anisotropic Electronic Characteristics, Adsorption, and Stability of Low-Index $BiVO_4$ Surfaces for Photoelectrochemical Applications. *ACS Appl. Mater. Interfaces* **2018**, *10*, 5475–5484. [CrossRef] [PubMed]
39. Cadelano, E.; Palla, P.L.; Giordano, S.; Colombo, L. Elastic Properties of Hydrogenated Graphene. *Phys. Rev. B* **2010**, *82*, 235414. [CrossRef]
40. Andrew, R.C.; Mapasha, R.E.; Ukpong, A.M.; Chetty, N. Mechanical properties of graphene and boronitrene. *Phys. Rev. B* **2012**, *85*, 125428. [CrossRef]
41. Lu, C.; Chen, C. Structure-strength relations of distinct MoN phases from first-principles calculations. *Phys. Rev. Mater.* **2020**, *4*, 44002. [CrossRef]
42. Li, Y.; Wang, H.; Xie, L.; Liang, Y.; Hong, G.; Dai, H. MoS_2 Nanoparticles Grown on Graphene: An Advanced Catalyst for the Hydrogen Evolution Reaction. *J. Am. Chem. Soc.* **2011**, *19*, 7296–7299. [CrossRef]
43. Lee, C.; Wei, X.; Kysar, J.W.; Hone, J. Measurement of the Elastic Properties and Intrinsic Strength of Monolayer Graphene. *Science* **2008**, *321*, 385–388. [CrossRef]
44. Lorenz, T.; Teich, D.; Joswig, J.; Seifert, G. Theoretical Study of the Mechanical Behavior of Individual TiS_2 and MoS_2 Nanotubes. *J. Phys. Chem. C* **2012**, *21*, 11714–11721. [CrossRef]
45. Zhang, S.; Zhou, J.; Wang, Q.; Chen, X.; Kawazoe, Y.; Jena, P. Penta-graphene: A new carbon allotrope. *Proc. Natl. Acad. Sci. USA* **2015**, *112*, 2372–2377. [CrossRef]

46. Xiao, W.; Xiao, G.; Rong, Q.; Wang, L. Theoretical discovery of novel two-dimensional V^{A}-N binary compounds with auxiticity. *Phys. Chem. Chem. Phys.* **2018**, *20*, 22027–22037. [CrossRef] [PubMed]
47. Kou, L.; Ma, Y.; Tang, C.; Sun, Z.; Du, A.; Chen, C. Auxetic and Ferroelastic Borophane: A Novel 2D Material with Negative Poisson's Ratio and Switchable Dirac Transport Channels. *Nano Lett.* **2016**, *16*, 7910–7914. [CrossRef]
48. Jong, M.D.; Chen, W.; Angsten, T.; Jain, A.; Notestine, R.; Gamst, A.; Sluiter, M.; Ande, C.K.; Zwaag, S.V.D.; Plata, J.; et al. Charting the complete elastic properties of inorganic crystalline compounds. *Sci. Data* **2015**, *2*, 150009. [CrossRef]
49. Liu, B.; Niu, M.; Fu, J.; Xi, Z.; Lei, M.; Quhe, R. Negative Poisson's ratio in puckered two-dimensional materials. *Phys. Rev. Mater.* **2019**, *3*, 54002. [CrossRef]
50. Jin, W.; Sun, W.; Kuang, X.; Lu, C.; Kou, L. Negative Poisson Ratio in Two-Dimensional Tungsten Nitride: Synergistic Effect from Electronic and Structural Properties. *J. Phys. Chem. Lett.* **2020**, *11*, 9643–9648. [CrossRef] [PubMed]